

Development of the Stanford GNSS Navigation Testbed for Distributed Space Systems

Vincent Giraldo, *Space Rendezvous Lab, Stanford University, Stanford, CA, United States*
Simone D'Amico, *Space Rendezvous Lab, Stanford University, Stanford, CA, United States*

BIOGRAPHY (IES)

Vincent Giraldo is a Ph.D. student in the Space Rendezvous Laboratory. He graduated from Bucknell University with a Bachelor of Science degree in mechanical engineering. His current research focuses on using GNSS technology for precise relative navigation of multiple small satellites. This includes development of algorithms for integer ambiguity resolution to accomplish this task in real-time, given the onboard constraints. His main research project is the Distributed multi-GNSS Timing and Localization system (DiGiTaL) under development for the NASA Small Satellite Technology Development Program in cooperation with NASA Goddard Space Flight Center and Tyvak Nanosatellite Systems.

Simone D'Amico is an Assistant Professor of Aeronautics and Astronautics at Stanford University, a Terman Faculty Fellow of the School of Engineering, Founder and Director of the Space Rendezvous Laboratory, and Satellite Advisor of the Student Space Initiative, Stanford's largest undergraduate organization. He received his B.S. and M.S. from Politecnico di Milano and his Ph.D. from Delft University of Technology. Before Stanford, Dr. D'Amico was at DLR, German Aerospace Center, where he gave key contributions to the design, development, and operations of spacecraft formation-flying and rendezvous missions such as GRACE (United States/Germany), TanDEM-X (Germany), and PRISMA (Sweden/Germany/France), for which he received several awards. Dr. D'Amico's research lies at the intersection of advanced astrodynamics, GN&C, and space system engineering to enable future distributed space systems. He has over 100 scientific publications including conference proceedings, peer-reviewed journal articles, and book chapters. He has been a Programme Committee Member (2008), Co-Chair (2011), and Chair (2013) of the International Symposium on Spacecraft Formation Flying Missions and Technologies. He is a Programme Committee Member of the International Workshop on Satellite Constellations and Formation Flying since 2013. He is a member of the Space-Flight Mechanics Technical Committee of the American Astronautical Society and Associate Editor of the Journal of Guidance, Control, and Dynamics.

ABSTRACT

Distributed Space Systems (DSS) promise advances in space science, earth and planetary science, as well as on-orbit servicing and space situational awareness. In order to mimic a large spacecraft with gigantic and reconfigurable aperture, DSS rely on precise knowledge of the relative position/velocity of the co-orbiting satellites. Especially in Earth's orbit, Global Navigation Satellite Systems (GNSS) can provide centimeter-level or better relative navigation solutions through differential carrier-phase processing techniques on cooperative satellites. The development of these GNSS functionalities and the verification of their capability to meet next-generation space mission requirements necessitate a high-fidelity testing environment. This research presents the design, development, and verification of the Stanford GNSS navigation testbed for spacecraft formation-flying and rendezvous. Key aspects of the system architecture are illustrated, including the orbital dynamics simulation, the GNSS signal and measurement generation, and the algorithms/software for advanced navigation applications. Each subsystem of the testbed is thoroughly verified through comparisons with flight data from space missions, live signals from static scenarios, and realistic hardware-in-the-loop simulations. Specifically, orbit propagation results are compared against precise flight dynamics products from the PRISMA formation-flying mission. A cross-verification method is introduced to validate the GNSS signal simulator and a software receiver emulator using a live signal source. In particular, an Extended Kalman Filter is used to quantify the distribution of pseudorange and carrier-phase measurement residuals from each signal source. The measurement residual statistics, along with satellite tracking performance, are then used as comparison metrics to verify that all stimulation methods are consistent with one another. After verification of the testbed, a commercial-off-the-shelf GNSS receiver is characterized using a zero-baseline test in order to quantify the measurement noise and assess its capability to support precision navigation on nanosatellites. Finally, the testbed is used to assess the

performance of the Distributed multi-GNSS Timing and Localization system (DiGiTaL), a precision navigation payload for small satellite swarms under development at Stanford in collaboration with NASA Goddard Space Flight Center.

INTRODUCTION

Distributed satellite systems use multiple spacecraft interacting in a coordinated manner to accomplish objectives that would be challenging, if not impossible, to achieve with a single large spacecraft. These systems have a variety of applications, including close-proximity operations such as on-orbit servicing and assembly [1], and science applications like exoplanet imaging [2] or synthetic aperture radar interferometry [3] to name a few. To fully exploit the scientific benefits of these missions, precise knowledge of the absolute and relative orbits of the cooperating spacecraft is required. Global Positioning System (GPS) receivers are recognized as the best device for providing onboard navigation wherever GPS signals are present. GPS navigation was successfully demonstrated for autonomous formation flying missions in Low Earth Orbit (LEO) by both PRISMA [4] and TanDEM-X [5], with the former demonstrating relative positioning errors less than 10 cm in most operational scenarios. As missions become increasingly reliant on GPS for navigation, realistic Hardware-In-the-Loop (HIL) testing of guidance, navigation, and control (GNC) functionalities based on GPS is critical to ensure the success of the mission.

As micro- and nano-satellites transition from being merely an educational tool to a viable scientific platform, many small satellite-based distributed mission concepts have been proposed [6]. One such mission is the CubeSat Proximity Operations Demonstration (CPOD), which will demonstrate rendezvous, proximity operations and docking (RPOD) using two 3-unit (3U) CubeSats weighing approximately 5 kg [7]. Due to the power, volume, mass, and cost constraints of small satellite systems such as CPOD, space-hardened receivers like the BlackJack [8] and the Integrated GPS Occultation Receiver (IGOR) [9] are not feasible options for onboard navigation. Therefore, Commercial-Off-The-Shelf (COTS) receivers are used in their stead. While COTS receivers provide many advantages over mission-specific devices, such as an increased number of channels, low power-consumption, and small volume and mass, there has not been a rigorous assessment of their viability for precise orbit determination and onboard navigation. This is a necessary step in assessing the feasibility of new small satellite mission concepts.

Additionally, new Global Navigation Satellite System (GNSS) constellations beyond GPS and GLONASS are becoming widely operational (e.g. Galileo, BeiDou), and the addition of new signals and frequencies presents the possibility to provide improvements in integer ambiguity resolution (IAR) and signal availability for above-the-constellation navigation [10]. Given the work-in-progress status of these constellations, their full potential can currently only be assessed in simulation.

A realistic HIL testbed enables stimulation of GNSS-based onboard navigation systems in a manner consistent with the flight environment. This is required for a critical assessment of the system performance since orbital scenarios present a uniquely challenging set of operational conditions for GNSS receivers that cannot be replicated on ground. Spaceborne GNSS receivers have to cope with large Doppler shifts, phase wind-up of the carrier signal, short tracking arcs, and rapidly varying constellation geometries. If the receiver firmware and the navigation algorithms are not properly adjusted to account for these conditions, the navigation performance could be severely degraded. By interfacing high-fidelity orbit propagation software with a GNSS signal simulator, it becomes possible to stimulate a receiver with radio frequency (RF) signals that are representative of what would be tracked on orbit.

The first closed-loop HIL testbed for GPS-based formation-flying, known as the Formation Flying Test Bed (FFTB), was created by Leitner [11] at Goddard Space Flight Center (GSFC). This testbed is capable of simulating GPS L1 and L2 frequencies for each of up to four spacecraft. The FFTB testbed has been used by Burns et al. [12] to demonstrate formation control, by Gill et al. [13] to simulate autonomous formation-flying, and by Winternitz [14] to validate the above-the-constellation GPS navigation system of the Magnetospheric Multi-Scale (MMS) mission. The German Space Operations Center developed a GPS-based HIL testbed that has been used extensively in the development of autonomous formation-flying capabilities. Leung [15] used the testbed to demonstrate relative navigation of a four-satellite formation, while D'Amico et al. [16-17] used it extensively for the development of the PRISMA autonomous navigation system. Other GPS testbeds include those of Kowalchuck [18] and Park et al. [19] which were developed to aid in formation-flying GNC research. More recently, Montenbruck et al. [20] and Biswas et al. [21] have used testbeds that are capable of simulating constellations other than GPS, specifically GLONASS and Galileo, to investigate single-satellite navigation algorithms.

This work presents the design, development, and use of the Stanford GNSS and Radiofrequency Autonomous Navigation Testbed for DSS (GRAND) for HIL testing of GNSS receivers and satellite navigation systems. The HIL testing system provides multiple methods for characterizing and testing GNSS receivers and related GNC algorithms. Multiple testing modes, each of increasing simulation complexity and fidelity, are available. In the most basic configuration, a

software receiver emulator is used to generate sets of GNSS measurements in faster-than-real-time allowing for rapid evaluation and iteration of navigation algorithms in different operational scenarios. More realistic testbed configurations seamlessly exchange the receiver emulator for an RF signal from either a rooftop antenna or a GNSS Signal Simulator (GSS). The antenna allows for testing with true GNSS signals from multiple constellations and frequencies, while the GSS allows for a user-defined environment with multiple RF outputs, giving flexibility in scenario definitions. The ability to reproduce a scenario observed by a static antenna with the receiver software emulator and the GSS provides a cross-validation baseline for each simulation method to ensure the fidelity and consistency between methods. The support of static test scenarios also enables GNSS receiver noise characterization through zero-baseline testing. In the most complex operational mode, orbits of multiple cooperating satellites are simulated in real-time and used by the GSS to generate representative RF signals for each trajectory.

The GNSS navigation testbed described in this paper will be used to support the design and testing of the Distributed multi-GNSS Timing and Localization (DiGiTaL) system under development at Stanford as part of the NASA Small Spacecraft Technology Program (SSTP) [22]. The goal of DiGiTaL is to provide nanosatellite formations with unprecedented, centimeter-level relative navigation accuracy in real-time and nanosecond-level time synchronization. This is achieved through the integration of a multi-GNSS receiver, a chip-scale atomic clock (CSAC), an intersatellite link (ISL) and on-board microprocessor for a total 0.5U volume CubeSat payload. To meet the strict requirements of future miniaturized distributed space systems, DiGiTaL exploits powerful error-cancelling combinations of synchronous carrier-phase measurements which are exchanged between the swarming nanosatellites through a peer-to-peer decentralized network. A reduced-dynamics estimation architecture on-board each individual nanosatellite processes the resulting millimeter-level noise measurements to reconstruct the full formation state with high accuracy. Through rigorous testing of two engineering units in both GRAND and FFTB at Stanford and GSFC, respectively, DiGiTaL will raise the technology readiness level (TRL) of precision navigation for small satellite formations from 3 to 6. In this paper, the HIL testing system at Stanford is used to validate prototype algorithms for the DiGiTaL satellite navigation system. Key results from the tests of prototype algorithms for absolute and relative navigation accuracy are presented and discussed.

SYSTEM ARCHITECTURE

The Stanford GNSS navigation testbed is designed for modularity and functionality. To accomplish this task, the testbed architecture is divided into multiple segments, including orbit/attitude dynamics simulation, GNSS signal and measurement generation, and navigation software and algorithms. Figure 1 depicts the testbed and the segmentation in a block diagram which highlights the data flow. Each segment is described in the subsequent sections.

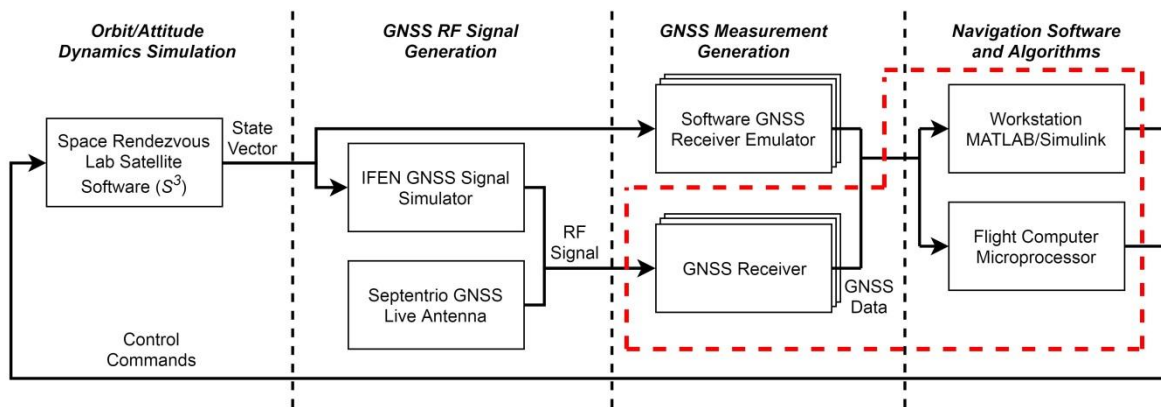


Figure 1: Schematic of GRAND. Test articles are outlined in red

Formally, the testbed includes any device and software used to evaluate test articles, namely flight hardware/software and navigation algorithms at large. In addition to the truth dynamics simulation, the GNSS signal generation, and a reference GNSS receiver for collection of data and cross-verification, the testbed includes the different environments that can house the GNC algorithms, such as a workstation or a nanosatellite microprocessor. The test articles are denoted in Figure 1 by the dashed red outline. These include GNSS receivers that are intended for flight as part of a satellite navigation payload, as well as GNC algorithms and software. The software can be embedded either in a MATLAB/Simulink environment or in a nanosatellite microprocessor.

Orbital Dynamics Simulation

The HIL testbed is designed to allow for hardware and algorithm deployment in an environment that realistically mimics the space environment. This requires simulation of the orbital and attitude dynamics by modeling all relevant forces and numerically integrating the resulting equations of motion. This precise simulation must occur in real-time to allow true evaluation of the navigation payload test article.

A custom-built software library was developed for dynamic simulation known as the Space Rendezvous Lab Satellite Software, also called S^3 . The software is written in C/C++ to limit computational overhead, and also simplifying the process of porting functionality to a flight computer. The software modules that comprise S^3 consist of time system conversion, reference system transformations, orbital and attitude perturbation models, and numerical propagators. S^3 is also made available in the MATLAB/Simulink environment through MEX function-wrappers and S-functions, where GNC algorithm research and development can occur in a more user-friendly language.

In order to use this software package for validation of orbit determination techniques, high-fidelity orbit perturbation models are necessary to create a representative space environment. An effort was made during the creation of S^3 to use the most recent state-of-the-art models. Table 1 lists the currently available models for use in testbed simulation.

Table 1: Orbit perturbation models, corrections, and reference frames supported by S^3

<i>Orbit Perturbation</i>	<i>Model</i>
Gravity Field	GGM01S (120x120) [23]
Atmospheric Drag	Harris-Priester [24] NRLMSISE-00 [25] (under development) Cannonball spacecraft model [24]
Solar Radiation Pressure	Flat plat model [24] Conical Earth Shadow model [24]
Geomagnetic & Solar Flux Data	NOA Daily KP AP Indices
Third-Body Perturbations	Analytical Sun & Moon [24] DE430 (All planets) [26]
Relativistic Corrections	First-order corrections for special and general relativistic effects [24]
Empirical Accelerations	First-order Gauss-Markov process [27]
<i>Reference Frames</i>	
Reference Frame	IAU 2010 [28-29]
Conventions	EME 2000 [24]
Precession/Nutation	IAU 2006/2000A [29] IAU 1980/1976 [24]
Earth Orientation	IERS EOP C04 14 [30]
Parameters	IERS EOP A 08 [28] IERS EOP B 08 [28]
Numerical Integration	Fourth-order Runge Kutta Dormand-Prince RK7(8) (under development)

GNSS Signal Generation

The Stanford testbed has two methods of generating RF signals for use in a GNSS receiver. The first is a live GNSS antenna statically mounted on the roof of the William F. Durand building at Stanford University. While the primary purpose of the testbed is to support orbital navigation system testing, the addition of static testing capabilities provides a check on other GNSS signal generation methods used in the testbed, ensuring they are properly functioning and calibrated. A Septentrio PolaNt Choke Ring B3/E6 antenna [31] was selected due to the choke ring feature, which provides improved multi-path rejection and low phase-center variation compared to a traditional patch antenna. This antenna is also compatible with the full range of GNSS signal bands and can be seen mounted on the roof in Figure 2.



Figure 2: Septentrio Choke Ring antenna mounted at Stanford University

The second method of signal generation is an IFEN NavX Professional multi-GNSS signal simulator [32]. This is the central component of the testbed that allows for the use of a GNSS receiver in hardware-in-the-loop orbital test cases by taking input trajectories from S^3 . The NavX Professional is capable of simulating 72 independent signals, divided between two independent RF outputs. The unit is currently able to simulate GPS L1, Galileo E1, BeiDou B1, QZSS, and IRNSS signals. Its capabilities can be further extended through a software license upgrade to include the L2, L5, E5a, E5b, E6, B2, and B3 signals. Figure 3 shows the GSS used in the Space Rendezvous Lab.



Figure 3: IFEN NavX multi-GNSS signal simulator (top) with a Septentrio AsteRx4 GNSS receiver OEM development board (bottom)

Although the IFEN GSS is a reliable commercial product, a verification step is necessary to show that it can produce RF signals that are representative of the signals received from the true GNSS constellations. Therefore, a cross-comparison between the GSS and live signals from the Septentrio antenna (see Fig. 2) is discussed in the Verification and Evaluation section of this paper.

GNSS Measurement Generation

The RF signals generated using the hardware described in the previous section can be used to create measurements through a GNSS receiver. Two receiver models were selected for testing and development. The first is part of the DiGiTaL system test article, and the second is used as a reference receiver for comparison.

To select which GNSS receiver was to be used with DiGiTaL, a survey of COTS receivers for use on small satellites was done. Criteria ranged from low power consumption (max 3W) and small board footprint (max 100mm²) to compatibility

with all current and planned GNSS constellations and frequencies. The selected receiver must also accept an external frequency reference (e.g., from an external clock), and preference was given to receivers who had flight heritage or whose predecessors had flight heritage. From this survey, the Novatel OEM628 High Performance GNSS Receiver was chosen [33].

A second receiver was chosen from the survey to be used as a reference. The Septentrio AsteRx4 GNSS receiver [34] was considered a suitable model for this purpose, due to the similar specifications to the Novatel. The functional difference between the two units is strictly mass and power. The Novatel has a mass of 37g and a power consumption of 1.3W, compared with 55g and 3W for the Septentrio. This difference makes the Novatel ideal for the DiGiTaL system which seeks compatibility with a CubeSat form factor, while the Septentrio was selected as reference receiver in a lab setting where mass and power constraints are less restrictive (see Figure 3). These two receivers take as input RF signals from either the rooftop antenna or the IFEN GSS, and output GNSS data, including pseudorange, carrier-phase, and broadcast ephemeris information.

Measurements can also be generated synthetically through the use of a GNSS Software Receiver Emulator (SRE). The receiver emulator takes as inputs the user state vector (from the dynamics simulation), the state vectors of the GNSS constellation satellites (from either International GNSS Service (IGS) Final Products [35] or RINEX ephemerides), and the current simulation time. All state vectors are provided in the Earth-Centered, Earth-Fixed (ECEF) frame, and all times are provided in GPS time, regardless of the actual GNSS constellation used. The emulator generates as outputs the pseudorange, carrier-phase, and Doppler shift measurements corrupted by path delays and receiver-specific noise for each GNSS constellation and frequency. A receiver emulator has the added benefit of being able to generate measurements in faster-than-real time, allowing for quick software-only testing and iteration of algorithms. The emulator uses a standard model of GNSS pseudorange, ρ_{pr} , and carrier-phase, ρ_{cp} , at time t , given by

$$\begin{aligned}\rho_{pr}(t) &= \|\mathbf{r}(t) - \mathbf{r}_{GNSS}(t - \tau)\| + c(\delta t - \delta t_{GNSS}) + I + T + \epsilon_{pr} \\ \rho_{cp}(t) &= \lambda\Phi = \|\mathbf{r}(t) - \mathbf{r}_{GNSS}(t - \tau)\| + c(\delta t - \delta t_{GNSS}) - I + T + \lambda N + \epsilon_{cp}\end{aligned}\quad (1)$$

In this model, \mathbf{r} is the position vector of the user's antenna and \mathbf{r}_{GNSS} is the position vector of the GNSS satellite's antenna (specifically the phase center of the antennae). The clock offset of both the receiver and the GNSS system are given by δt and δt_{GNSS} , respectively. This model includes the effects of signal time-of-flight, τ , Ionospheric path delay, I , Tropospheric path delay, T , and the added uncertainty of integer ambiguities, N , which is multiplied by the wavelength of the incoming signal, λ . These values are dependent on the scenario definition, and independent of the hardware used. Note that this model neglects receiver and channel dependent biases, as well as phase wind-up on the carrier-phase. However, the receiver-specific noise values, ϵ_{pr} and ϵ_{cp} , remain uncertain quantities.

Every physical GNSS receiver is subject to measurement errors due to thermal noise in the electronics, signal tracking errors introduced by the delay- and phase-lock-loop settings, and manufacturing variations. These noise values vary not just between receiver models, but also between individual units. They are impossible to know a-priori and can only be quantified through hardware characterization. To develop a rigorous simulation of all components, the hardware receiver being emulated in software must be incorporated into the testbed and stimulated with RF signals, either by an antenna or by a GSS. This allows for a zero-baseline test to be conducted to quantify the receiver-specific noise. This characterization method is performed on the Septentrio AsteRx4, and is discussed in the Verification and Evaluation section.

Navigation Software and Algorithms

The final block of the testbed contains the GNC software, which will use the GNSS measurements provided by the previous segment to determine the state of the spacecraft and command any necessary maneuvers. For the purpose of algorithm development, the software can be used on a workstation in the MATLAB/Simulink environment. This enables functionality testing of new methods and algorithms. To test how well the software performs in real-time under onboard constraints, it can be written in C/C++ and embedded to a nanosatellite microprocessor. Processor-in-the-loop testing is the final stage of software development, and completes the HIL testbed.

For the testing and design of the DiGiTaL system, two development boards were acquired from Tyvak Nanosatellite Systems. These boards, also known as flatsats, contain relevant hardware in an environment that mimics a small spacecraft. The flatsats consist of the Novatel OEM628 GNSS receiver, a flight processor, and a UHF radio for communication of measurements and state information between the two units. Other components of the development boards aid in the interfacing with the units, specifically through a secondary processor for command and data handling (C&DH). A chip-scale atomic clock (CSAC) produced by Jackson Labs [36] was also selected for future integration into the development boards. This clock will be used to condition the GNSS receiver, reducing clock drift during GNSS-impaired scenarios, as well as improving synchronization between multiple DiGiTaL units. Figure 4 shows the two flatsats with labelled components, and the selected CSAC.

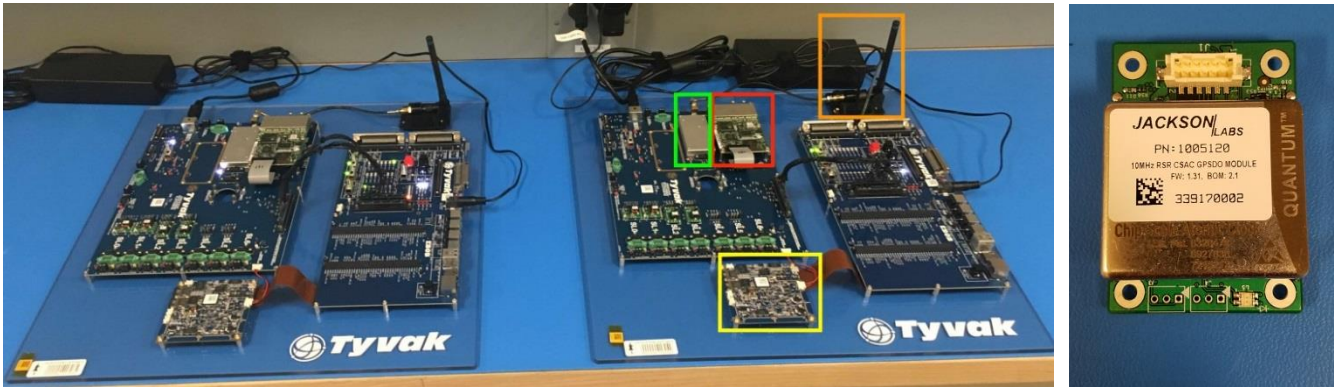


Figure 4: Two prototype DiGiTaL units (left), including the flight processor (yellow), UHF radio (green), Novatel receiver (red), and intersatellite link antenna (orange), and a chip-scale atomic clock (right)

The flight processor will house the GNC algorithms for DiGiTaL, and can later be used as a test computer to run additional software for other projects to test their feasibility as flight software. The specifications of this microprocessor, as well as the UHF intersatellite link and C&DH processor, are given in Table 2.

Table 2: Specifications of flatsat development board processors and UHF intersatellite link

<i>Onboard Processors</i>		<i>UHF Radio</i>	
<i>Command & Data Handling Processor</i>		Frequencies	400-470 MHz
Architecture	ARM9		800-930 MHz
Clock speed	400 MHz	Data Rates	1.2 250 kbps
Power Consumption	< 0.2 W	<i>Power Consumption</i>	
<i>GNC Application Processor</i>		RF TX	Up to 2 W
Architecture	ARM Cortex A8+	DC TX	7 W
Clock Speed	800 MHz	DC RX	0.130 W
Mass	610 g	Mass	20 g
Volume	83 x 83 x 53 mm	Volume	32 x 87 x 8 mm
Power Consumption	< 1 W	Power Consumption	< 1.3 W

Open and Closed-Loop HIL Testing

To allow for a variety of testing scenarios, the testbed can be utilized in both open-loop and closed-loop simulation configurations. An open-loop configuration is defined as having no orbit or attitude maneuvers computed by the spacecraft GNC system in real-time as a function of the state. Therefore, the complete orbital trajectory is determined by the initial conditions and can be precomputed. This does not allow for validation of a full GNC system since the guidance and control algorithms have no effect on the spacecraft trajectory. However, the closed-loop configuration allows for maneuvers to be computed in real-time based on the navigation solution and fed back into the propagation to test the guidance and control algorithms. This integrated test configuration is able to assess the strongly coupled behavior of navigation and orbit control systems.

The testbed had to be developed in such a way to realize either open- or closed-loop testing capabilities. First, a custom-built workstation is used to host all environmental simulation as well as to configure the test settings. The host workstation also serves to host any receiver emulators as well as monitor the simulation status. A second computer is also introduced to mimic ground-station functionality such as sending telecommands to the test article over TCP/IP and downlinking any telemetry.

It is also essential to synchronize the dynamics simulation with the GSS. This synchronization is accomplished through the addition of a Spectracom TSync Timing Card [37] to the workstation. The timing card can transmit and receive 1PPS 3V TTL or 10 MHz reference signals and use these signals to condition the simulation clock to be in sync with the GSS. If a timing card is not included, a drift between the two device clocks would occur. The trajectory data exchanged between the software simulation and the GSS would become inconsistent over time, causing invalid measurements to be created. This delay and resulting inconsistency are not acceptable for rigorous validation of GNC flight software, especially for simulations of several hours.

VERIFICATION AND EVALUATION

Before the testbed can be used to analyze flight hardware, algorithms, and full GNC payloads, it must itself be verified to ensure it functions as expected. This includes validation of orbit simulation models, verification of all methods of GNSS measurement generation, and evaluation of the reference GNSS receiver.

Comparison against Flight Dynamics Products

The HIL testbed provides a powerful tool for simulating the orbit of a spacecraft with all relevant perturbations through the S^3 software package. The orbit propagator of S^3 was validated by comparing it with PRISMA flight data, which show absolute and relative orbit accuracy on the meter- and centimeter-level, respectively [38-39]. A series of one-hour propagations using S^3 were performed given initial conditions from flight products, and comparisons were made over each of the arcs between the propagated orbit and the true orbit. Extensive comparison showed that numerical integration of the equations of motion in S^3 provided accuracy to the level of the PRISMA products. As an example, Figure 5 shows the resulting propagation error for both the absolute and relative orbits using products from March 17, 2011. The mean final errors over all of the propagation arcs were 1.84 m and 0.10 m for absolute and relative orbits, respectively.

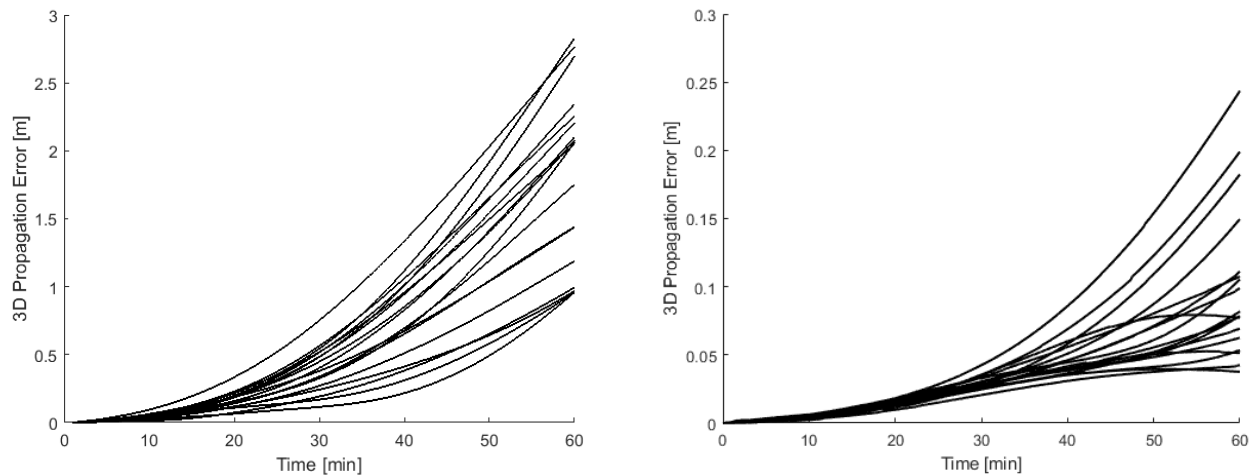


Figure 5: 3D error using the S^3 orbit propagator compared against PRISMA flight dynamics orbit products for absolute (left) and relative (right) navigation

Cross-Comparison for Static Test Environment

The methods of generating GNSS measurements also required verification to ensure confidence in the testbed. To confirm that all methods accurately produce the measurements that would be expected in reality, a cross-comparison was done between the Software Receiver Emulator (SRE), the IFEN GSS, and the live Septentrio antenna. The latter two items were connected to the Septentrio AsteRx4 reference receiver to convert the RF signals into GNSS observables.

To begin the cross-comparison, the live antenna and receiver were used to collect what is considered the truth observables for the test. This data contains broadcast ephemerides and an observation file with pseudorange, carrier-phase, Doppler measurements, and signal carrier-to-noise ratios (C/N_0). To extract a precise position from this data, the observation file was processed using the Natural Resources Canada's (NRC) fast precise-point positioning (PPP) service [40-41]. This is a user-friendly service provided by the Canadian government for a variety of applications, including surveying, mapping, and navigation. Precise orbit products for the GNSS satellites are used in conjunction with the measurements in the observation file to create a baseline position estimate accurate to the centimeter-level.

Comparison tests were then set up by recreating this static scenario using both the SRE and GSS for environmental simulation and measurement generation. To accurately match the test conditions, the state of the GNSS constellations had to be carefully reproduced. Precise orbit products were retrieved from the IGS, which provide the GNSS satellite locations currently accurate to 2.5 cm for GPS and 20 cm for BeiDou and Galileo [35]. The testbed scenario also includes the Ionospheric path delay, modeled using Klobuchar constants from the broadcast ephemeris information, and Tropospheric path delay, as well as a model of the antenna gain pattern. Table 3 describes the scenario parameters that were used for both the SRE and the GSS tests.

Table 3: Static test configuration settings

<i>Parameter</i>	<i>Value</i>
Initial Epoch	April 21, 2017, 00:00:00 GPST
Final Epoch	April 22, 2017, 00:00:00 GPST
Latitude	37° 25' 36.9852"
Longitude	-122° 10' 23.7379"
Altitude	19.899 m
GNSS Systems	GPS, GAL, BDS

Tests were conducted to compare the rooftop live antenna, SRE, and the GSS, and the validity of each signal generation method was analyzed. The live antenna test was used as a reference because no simulation is done in this case, and all the information is coming from the true GNSS satellites. The SRE and GSS tests were then compared against the live antenna test, and three metrics were used: satellite tracking, signal C/N₀, and the navigation solution. Satellite tracking was analyzed by use of a skyplot, which shows the trajectories of each GNSS satellite as a function of the azimuth and elevation with respect to the antenna's ground plane. The skyplots from each test are shown in Figure 6.

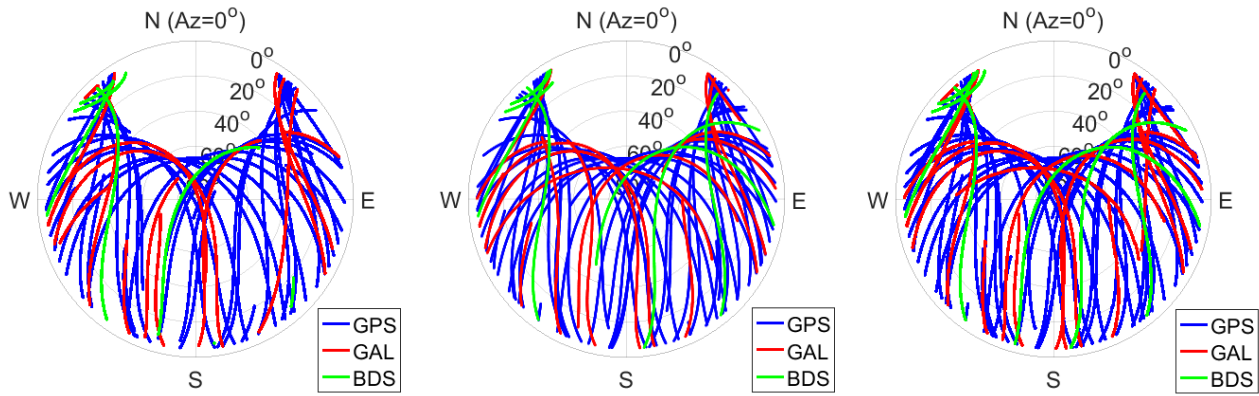


Figure 6: Tracked satellite trajectories with respect to the antenna plane from rooftop live antenna test (left), SRE test (center), and GSS test (right)

Compared to the live test, the SRE and GSS tests show 2 more BeiDou satellites and 4 more Galileo satellites being tracked, particularly for lower elevations. The SRE and GSS tests show nearly identical satellite tracking. This suggests that either there are line-of-sight obstructions preventing the live antenna from receiving low-elevation signals, or both the SRE and GSS are neglecting low elevation signal-propagation effects. However, the vast majority of tracked satellites are the same between tests, providing a first positive confirmation of each testing method.

The second simulation-consistency metric is the signals' carrier-to-noise ratios. Figure 7 shows the C/N₀ as measured by the receiver in each case. As expected, there is a decrease in C/N₀ with decreasing elevation, which is a result of decreased antenna gain at low elevations. Differences between the three tests occur near the lowest elevations, specifically less than 20 degrees. In the live test, there is a variation in noise of 15 dB-Hz at these elevations, compared with 5 dB-Hz in the SRE and GSS tests. This is attributed to un-modeled multi-path effects. Although the antenna was selected such to mitigate these effects, it cannot completely remove them. Since these effects were assumed to be small, the simulation scenarios were defined without multi-path. This indicates that for orbital scenarios where multi-path effects may be present (possibly due to deployable solar panels and close-by satellites), it will be necessary to include multi-path effects in simulation due to their effect on measurement noise.

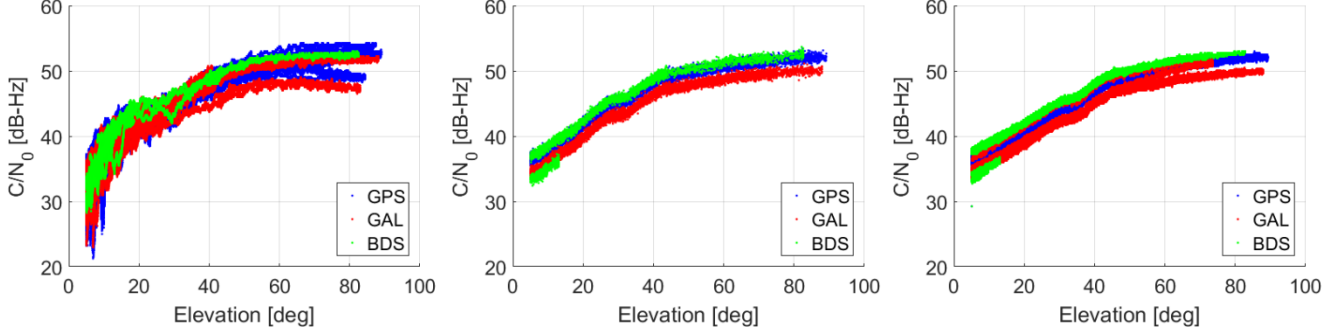


Figure 7: Signal carrier-to-noise ratio from rooftop live antenna test (left), SRE test (center), and GSS test (right)

The final cross-comparison between live antenna, SRE, and GSS stimulation methods was done by evaluating the accuracy of the navigation solution from each test. To this end, an Extended Kalman Filter (EKF) was developed and used with each test, taking as inputs the raw measurements (pseudorange and carrier-phase), and outputting a static position estimate. The following describes the development of the EKF used in the analysis. A similar approach is used for orbital scenarios in the following of the paper.

The pseudorange and carrier-phase measurement models are presented in Equation 1. To eliminate Ionospheric delays, the Group and Phase Ionospheric Calibration (GRAPHIC) [42] measurements were formed from the combination of the code and phase measurements, as given by

$$\rho_{gr}(t) = \frac{\rho_{pr}(t) + \rho_{cp}(t)}{2} = \|\mathbf{r}(t) - \mathbf{r}_{GNSS}(t - \tau)\| + c(\delta t - \delta t_{GNSS}) + T + \lambda \frac{N}{2} + \epsilon_{gr} \quad (2)$$

where $\epsilon_{gr} \approx 0.5\epsilon_{pr}$. Although the Ionospheric delay has been eliminated, the Tropospheric delay term is still present and must therefore be modeled. This is accomplished through the Minimum Operational Performance Standards (MOPS) [43] model, which divides the delay into dry hydrostatic, $T_{z,dry}$, and wet-zenith delay, $T_{z,wet}$, components. These delays are then mapped to different elevations using the Neill mapping function [44] as follows

$$T = T_{z,dry}M_{dry} + T_{z,wet}M_{wet} \quad (3)$$

where T is the total Tropospheric delay, and M represents the mapping functions. To account for variations in the wet delay component, which varies based on local weather conditions, the zenith wet delay is augmented with a correction factor, $\Delta T_{z,wet}$, modeled as a random walk process, given by

$$T_{z,wet} = T_{z0,wet} + \Delta T_{z,wet} \quad (4)$$

At this point, the full estimation state can be written as

$$\mathbf{x} = [\mathbf{r} \quad \mathbf{c}\delta\mathbf{t} \quad \mathbf{N} \quad \Delta T_{z,wet}]^T \quad (5)$$

where \mathbf{r} is the Earth-Centered, Earth-Fixed Cartesian coordinates of the antenna phase center, $\mathbf{c}\delta\mathbf{t}$ is the vector of receiver clock offsets with respect to each GNSS constellation time, \mathbf{N} is the vector of real-valued carrier-phase biases for each tracked signal, and $\Delta T_{z,wet}$ is the Tropospheric adjustment. For a filter using GPS (30 satellites), Galileo (14 satellites), and BeiDou (13 satellites), \mathbf{x} becomes a 64-dimensional state.

Since the antenna position is known to be fixed, and all other state variables are modeled as random-walk processes or constants, the state transition matrix Φ_{t,t_0} for the time-update simplifies to the identity matrix

$$\Phi_{t,t_0} = \frac{\partial \mathbf{x}_t}{\partial \mathbf{x}_{t_0}} = \mathbf{I}_{64 \times 64} \quad (6)$$

where \mathbf{x}_t and \mathbf{x}_{t_0} describe the state at time t and t_0 respectively, and \mathbf{I} is a 64-by-64 identity matrix.

The variance of the variables modeled as random walks is described by

$$q_i = \frac{\sigma_i^2(t-t_0)}{\tau_i} \quad (7)$$

which is added as process noise to the filter. The subscript i represents the given variable (either the clock offset, $\mathbf{c}\delta t$, or the Tropospheric correction, $\Delta T_{m,wet}$), and τ is the process-specific auto-correlation time constant.

For the measurement update phase of the EKF, the measurement sensitivity matrix, H , describes the expected change in measurement due to a change in state. It is calculated as the partial derivatives of the measurement model with respect to the state. For GRAPHIC measurements the sensitivity matrix is given by

$$\mathbf{H}_t = \frac{\partial z_t}{\partial x_t} = \left[-\mathbf{e} \quad \mathbf{1} \quad \frac{\lambda}{2} \quad M_{wet} \right]_{1 \times 64} \quad (8)$$

where z is the modeled measurement. The partial with respect to the clock offset takes a value of 1, and the partial with respect to the carrier-phase bias is half the wavelength, $\lambda/2$. The partial of the measurements with respect to the range is given as the negative of the line-of-sight vector from the satellite to the receiver [45]. The first-order approximation of this vector is given by

$$\frac{\partial z_t}{\partial r_t} = -\mathbf{e} = -\frac{\mathbf{r}_{GNSS}-\mathbf{r}}{\|\mathbf{r}_{GNSS}-\mathbf{r}\|} \quad (9)$$

The input parameters for the EKF, shown in Table 4, were the same for all conducted tests.

Table 4: Extended Kalman Filter parameters

<i>Parameter</i>	<i>Value</i>	<i>Parameter</i>	<i>Value</i>
<i>A-priori standard deviation</i>		<i>Process noise</i>	
σ_r [m]	10.0	$\sigma_{c\delta t}$ [m]	1.0
$\sigma_{c\delta t}$ [m]	10.0	$\sigma_{\Delta T_{m,wet}}$ [m]	0.1
σ_N [cycles]	5.0	<i>Measurement standard deviation</i>	
$\sigma_{\Delta T_{m,wet}}$ [m]	0.1	σ_{gr} [m]	0.5
<i>Auto-correlation time scale</i>			
$\tau_{c\delta t}$ [s]	100.0		
$\tau_{\Delta T_{m,wet}}$ [s]	1000.0		

This method of estimation was used to determine the location of the roof antenna. The ECEF position estimates from each test are shown in Figure 8. Here, the ground truth position is subtracted from the state estimate to form the error. Comparing the solution from the live antenna data, the SRE test, and the GSS test, the maximum mean error in one direction is 0.48 m. This value is on the order of the broadcast ephemeris error, and therefore can be seen as the lower bound on navigation accuracy when the broadcast ephemerides are used to provide GNSS constellation information instead of IGS precise orbit products. If the precise products are used, the lower bound on positioning accuracy would be on the centimeter-level, based on the accuracy of those products [35]. The error-bounds for each test are also consistent, with a maximum of 7 mm difference between any two tests in a given direction. Each test shows maximum variance in the y-component, and minimum variance in the x-direction. In topocentric coordinates, this corresponds to a maximum uncertainty in altitude, as expected.

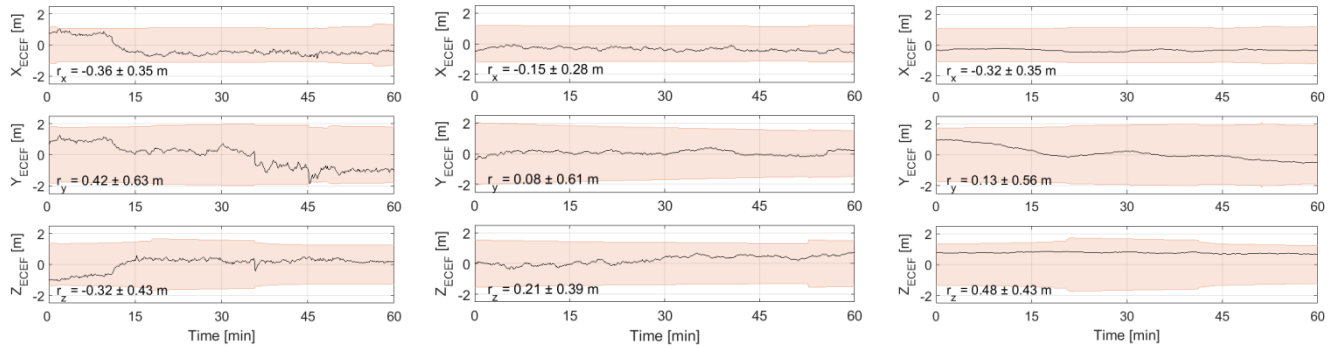


Figure 8: Position errors with 3σ bounds for a 1-hour arc from rooftop live antenna test (left), SRE test (center), and GSS test (right)

The filter output can also be compared in terms of post-fit residuals. The residuals for each test, shown in Figure 9, display a consistent band of white noise with standard deviations of approximately 12 cm. There are a few instances of higher residuals, which occur when a new satellite enters into view. This causes the filter to initialize and estimate a new carrier-phase bias. The standard deviation on the residuals is representative of the noise of the AsteRx4 receiver for GRAPHIC measurements. This is better shown in the next subsection, where the noise of the receiver is quantified through a zero-baseline test.

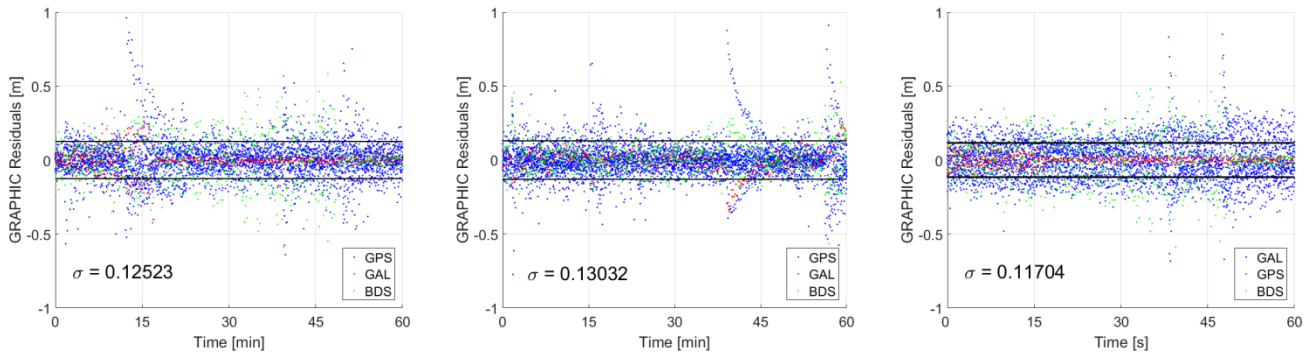


Figure 9: GRAPHIC measurement post-fit residuals from rooftop live antenna test (left), SRE test (center), and GSS test (right)

COTS Receiver Characterization

On-board GNSS-based satellite navigation systems have been able to achieve meter- and decimeter-level precision in absolute and relative positioning, respectively, in real-time. The ultimate lower-bound for real-time GNSS navigation accuracy, however, is determined by the noise of the used receiver. This drives the need to characterize the receiver to quantify the noise levels, which are required inputs to any EKF.

The quantification of receiver noise is accomplished through a process known as zero-baseline testing [46]. To perform this test, a receiver must be stimulated with two exact reproductions of the same scenario. Typically a live signal is simultaneously fed to two identical receiver units, characterizing the noise of that receiver model. While this is impossible to do for an individual unit using live signals, it can be accomplished using a GNSS signal simulator. It was previously shown that the IFEN GSS can be reliably used to replicate a live antenna scenario, and is therefore appropriate for use in a zero-baseline test. The presented work shows the characterization of the Septentrio AsteRx4, but can be identically repeated for any GNSS receiver.

To start, two identical scenarios must be run consecutively. The scenarios are configured to be error-free to eliminate any chance for unwanted deviations between the two tests. This entails removing atmospheric delays and broadcast ephemeris errors. The simulated antenna location was placed in Hong Kong to maximize the number of BeiDou geostationary and inclined geosynchronous satellites that were in view.

The measurements from the two tests are combined to form double-differenced combinations. This is accomplished by first creating single-differenced values, given for pseudorange measurements by

$$\begin{aligned}
\rho_{sdpr}^{(k)} &= \rho_{pr,u}^{(k)} - \rho_{pr,w}^{(k)} \\
&= (\|\mathbf{r}_u^{(k)}(t) - \mathbf{r}_{GNSS}^{(k)}(t - \tau)\| + c(\delta t_u - \delta t_{GNSS}^{(k)}) + I_u^{(k)} + T_u^{(k)} + \epsilon_{pr,u}^{(k)}) \\
&\quad - (\|\mathbf{r}_w^{(k)}(t) - \mathbf{r}_{GNSS}^{(k)}(t - \tau)\| + c(\delta t_w - \delta t_{GNSS}^{(k)}) + I_w^{(k)} + T_w^{(k)} + \epsilon_{pr,w}^{(k)}) \\
&= \|\mathbf{r}^{(k)}(t) - \mathbf{r}_{GNSS}^{(k)}(t - \tau)\|_{uw} + c\delta t_{uw} + I_{uw}^{(k)} + T_{uw}^{(k)} + \epsilon_{pr,uw}^{(k)}
\end{aligned} \tag{10}$$

The superscript k denotes measurements coming from GNSS satellite k , and the subscripts u and w represent measurements being taken by receivers u and w , respectively. Forming the single difference eliminates any terms that only depend on the observed GNSS satellite, which in this case is the clock offset of that satellite and broadcast ephemeris errors.

By collocating the receivers in each test, any terms that depend on geometric conditions cancel out. This includes the range from the receiver to the transmitting satellite and atmospheric effects, although the latter were not included in the simulation. The reduced single-difference pseudorange equation is given by

$$\rho_{sdpr}^{(k)} = c\delta t_{uw} + \epsilon_{pr,uw}^{(k)} \tag{11}$$

A similar equation can be expressed for carrier-phase measurements, with the only difference being the inclusion of the carrier-phase bias. It is important to note that this bias is independent for each received signal.

$$\rho_{sdcp}^{(k)} = c\delta t_{uw} + \lambda N_{uw}^{(k)} + \epsilon_{cp,uw}^{(k)} \tag{12}$$

These single-difference combinations for satellites k and l are then differenced to form the double-differenced observations. This combination eliminates all terms from the incoming signals with the exception of the noise, which is a product of the receiver. The resulting double-difference is given by

$$\begin{aligned}
\rho_{ddpr}^{(k,l)} &= \rho_{sdpr}^{(k)} - \rho_{sdpr}^{(l)} \\
&= (c\delta t_{uw} + \epsilon_{pr,uw}^{(k)}) - (c\delta t_{uw} + \epsilon_{pr,uw}^{(l)}) \\
&= \epsilon_{pr,uw}^{(k,l)}
\end{aligned} \tag{13}$$

For the carrier-phase, this reduction still includes the bias term. However, N is known to have an integer value, and can thus be easily determined and removed to leave only the noise term.

$$\begin{aligned}
\rho_{ddcp}^{(k,l)} &= \rho_{sdcp}^{(k)} - \rho_{sdcp}^{(l)} \\
&= (c\delta t_{uw} + \lambda N_{uw}^{(k)} + \epsilon_{cp,uw}^{(k)}) - (c\delta t_{uw} + \lambda N_{uw}^{(l)} + \epsilon_{cp,uw}^{(l)}) \\
&= \epsilon_{pr,uw}^{(k,l)}
\end{aligned} \tag{14}$$

These double-differenced signals are formed between all satellites at a given epoch that have the same C/N_0 . Once a large number of these samples have been accumulated, the standard deviation can be calculated for the double-differenced measurements, which in turn can be related back to the un-differenced standard deviation by

$$\begin{aligned}
\sigma_{pr} &= \frac{\sigma_{ddpr}}{2} \\
\sigma_{cp} &= \frac{\sigma_{ddcp}}{2}
\end{aligned} \tag{15}$$

Noise values determined using the previously described experimental method can be compared against an analytical model for verification, which is given by [47]

$$\begin{aligned}
\sigma_{pr} &= \frac{c}{1.023 \times 10^6} \sqrt{\frac{b_{dpl}}{SNR}} \\
\sigma_{cp} &= \frac{\lambda}{2\pi} \sqrt{\frac{b_{ppl}}{SNR}} \\
SNR &= 10^{\frac{C/N_0}{10}}
\end{aligned} \tag{16}$$

This is a function of the signal-to-noise ratio SNR and the bandwidths of the tracking loops b .

The receiver noise for the pseudorange and carrier-phase measurements obtained experimentally by the previous approach is shown in Figure 10. The trends for both measurements match closely with the analytical solution from Equation 16. The level of pseudorange noise is <35 cm, with the mean value of 20 cm being approximately double that of the measurement residuals seen during the static receiver testing (see Fig. 9). This is precisely what is expected when using GRAPHIC measurements in the filter. The carrier-phase noise values of the AsteRx4 receiver are on the order of 1 mm, confirming its suitability for use with precision navigation of small satellites.

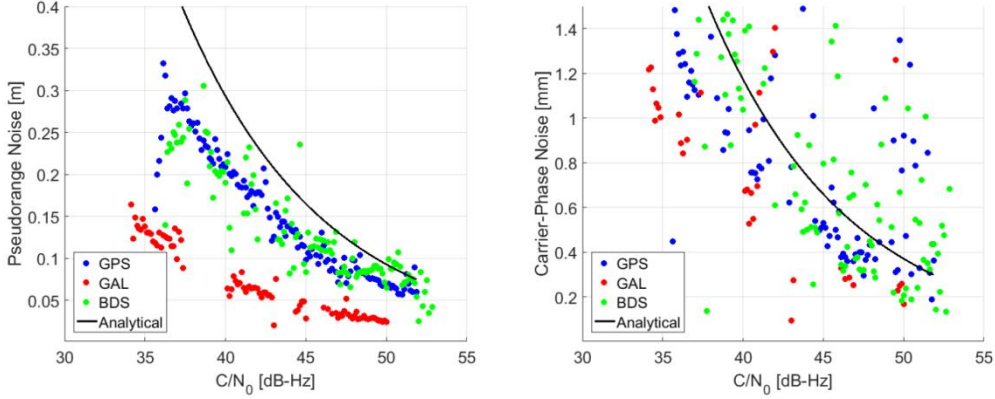


Figure 10: Measurement noise of Septentrio AsteRx4 receiver for pseudorange (left) and carrier-phase (right) as functions of the signal carrier-to-noise ratio

Distributed multi-GNSS Timing and Localization System

Once developed, the testbed can be used to analyze navigation software of a test article, specifically DiGiTaL. The goal of the DiGiTaL system is to provide a swarm of small satellites with cm-level relative positioning accuracy between every spacecraft. This is accomplished by utilizing differential carrier-phase GNSS (dGNSS), where measurements from multiple receivers are combined to cancel common errors in order to achieve highly precise relative measurements. Each spacecraft in the swarm will be equipped with a DiGiTaL unit, creating a decentralized architecture where every satellite will be estimating the state of the entire swarm. To accomplish this task, DiGiTaL employs a multi-inertial EKF that estimates the absolute state of each spacecraft. The filter uses GRAPHIC and single-difference carrier-phase (SDCP) measurements, which, for an orbital application, are given by

$$\rho_{gr}(t) = \|\mathbf{r}(t) - \mathbf{r}_{GNSS}(t - \tau)\| + c(\delta t - \delta t_{GNSS}) + \lambda \frac{N}{2} + \epsilon_{gr} \quad (17)$$

and

$$\rho_{sdcp}(t) = \|\mathbf{r}^{(k)}(t) - \mathbf{r}_{GNSS}^{(k)}(t - \tau)\|_{uw} + c\delta t_{uw} + \lambda N_{uw}^{(k)} + \epsilon_{sdcp}^{(k)} \quad (18)$$

respectively. These formulations are similar to those presented previously (Equations 2 and 12). However, Tropospheric delays are not present in low Earth orbit, removing them from the GRAPHIC equation, and the relative positions of the two spacecraft must be taken into account when formulating the SDCP equation.

Each filter will have one set of GRAPHIC measurements for every spacecraft, and one set of SDCP measurements for every pair of satellites. For an arbitrarily large swarm of N satellites, the number of measurements that have to be used grows proportional to N^2 . It is, therefore, infeasible to perform a filter measurement update for more than a few satellites. To accomplish full swarm estimation, a different approach is utilized. The swarm is divided into smaller subsets of 2 to 3 satellites, where an EKF will use dGNSS to estimate the states of the satellites in the subset by sharing measurements. This state and covariance information is transmitted to the rest of the swarm via an ISL, and then combined to create full swarm knowledge. State information can be combined through simple vector algebra, or more sophisticated methods such as covariance intersection. This method of dividing the swarm reduces the computational load of performing a measurement update by reducing the size of the necessary matrix inversion. The resulting measurement vector for a subset of two satellites is given by

$$\mathbf{z} = [\boldsymbol{\rho}_{gr}^u \quad \boldsymbol{\rho}_{gr}^w \quad \boldsymbol{\rho}_{sdcp}^{uw}]^T \quad (19)$$

which consists of a set of GRAPHIC measurements for satellites u and w , and a set of SDCP measurements between u and w . The state that the filter is estimating is given by

$$\mathbf{x} = [\mathbf{r}_u \quad \mathbf{v}_u \quad \mathbf{a}_u^{emp} \quad \mathbf{c}\delta\mathbf{t}_u \quad \mathbf{N}_u \quad \mathbf{r}_w \quad \mathbf{v}_w \quad \mathbf{a}_w^{emp} \quad \mathbf{c}\delta\mathbf{t}_w \quad \mathbf{N}_w]^T \quad (20)$$

where \mathbf{r} and \mathbf{v} are the position and velocity of each spacecraft center of mass in the Earth-centered inertial (ECI) frame and \mathbf{a}^{emp} is the empirical acceleration vector aligned in the radial R , along-track T , and cross-track N directions. The clock offset $\mathbf{c}\delta\mathbf{t}$ and carrier-phase bias \mathbf{N} vectors are defined in the previous subsection. The filter estimates the carrier-phase bias as float values, and then IAR is performed using the Modified LAMBDA method [48]. This method was selected due to its reduced complexity and computational load compared to the original LAMBDA method. When the biases are fixed, the corresponding covariance entries are set to zero, since these values are considered known over the tracking arc.

The time update of the filter is performed by numerically integrating the equations of motion to propagate the spacecraft state forward. However, due to onboard computational constraints, a reduced-dynamics model is employed. This model can be specified by the user, and can be tailored to the environment faced by the spacecraft. To aid in the propagation, the empirical accelerations estimate un-modeled dynamics and are included in the equations of motion. These terms are modeled as first-order Gauss-Markov processes.

The DiGiTaL navigation filter can be tested and validated in the HIL testbed. A four-spacecraft swarm scenario was simulated using S^3 , and then the trajectories were fed to the IFEN GSS for signal generation. The Septentrio AsteRx4 receiver was connected to the GSS to collect measurements for use in the filter, and all navigation software was run in the MATLAB/Simulink environment. Due to the desire to test navigation algorithms, no control maneuvers were executed over the course of the simulation. The spacecraft were simulated in orbits representative of a synthetic aperture radar interferometry mission. Figure 11 shows the orbits of the satellites in the RTN-frame of the first satellite, and their orbital elements are given in Table 5.

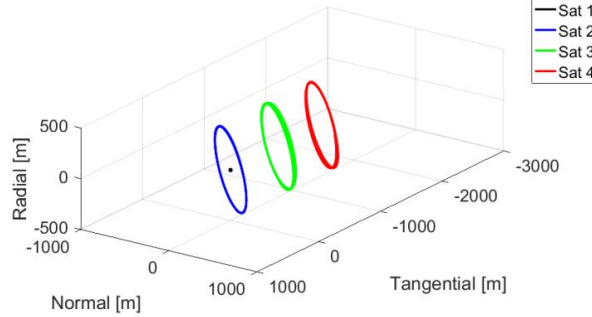


Figure 11: DiGiTaL test scenario simulated orbits in RTN frame of satellite 1

Table 5: Absolute orbital elements of satellite 1 and relative orbital elements of satellites 2-4 with respect to satellite 1

<i>Absolute Orbital Elements</i>	<i>Satellite 1</i>	<i>Relative Orbital Elements</i>	<i>Satellite 2</i>	<i>Satellite 3</i>	<i>Satellite 4</i>
Semi-Major Axis (a) [km]	7070.863	Relative Semi-Major Axis ($a\delta a$) [m]	-1.175	2.319	4.889
Eccentricity (e) [-]	6×10^{-4}	Relative Mean Longitude ($a\delta\lambda$) [m]	-0.743	753.362	-1491.197
Inclination (i) [°]	98.193	Relative Eccentricity ($a\delta e_x$) [m]	1.396	-260.173	254.644
Longitude of Ascending Node (Ω) [°]	0.588	Relative Eccentricity ($a\delta e_y$) [m]	301.320	-149.706	-152.073
Argument of Perigee (ω) [°]	-8.964	Relative Inclination ($a\delta i_x$) [m]	0.123	-519.516	519.041
Mean Anomaly (M) [°]	227.894	Relative Inclination ($a\delta i_y$) [m]	599.593	-302.051	-297.804

To implement the DiGiTaL filter, the swarm was divided into subsets, with each spacecraft estimating its own state plus that of one other satellite. The estimation topography is given in Table 6.

Table 6: Estimation subsets for DiGiTaL test scenario

<i>Spacecraft</i>	<i>Estimation Subset</i>
1	1,2
2	2,3
3	3,4
4	4,1

The reduced dynamics model for this filter includes only a 20x20 spherical harmonic gravity model, while the truth simulation includes the perturbations listed in Table 1. The input parameters for the EKF are shown in Table 7.

Table 7: Extended Kalman Filter parameters for DiGiTaL system

<i>Parameter</i>	<i>Value</i>	<i>Parameter</i>	<i>Value</i>
<i>A-priori standard deviation</i>		<i>Process noise</i>	
σ_r [m]	1000	σ_{aR} [nm/s ²]	7500
σ_v [m/s]	1	σ_{aT} [nm/s ²]	1000
σ_{aR} [nm/s ²]	1000	σ_{aN} [nm/s ²]	500
σ_{aT} [nm/s ²]	2000	$\sigma_{c\delta t}$ [m]	5
σ_{aN} [nm/s ²]	750	σ_N [cycles]	0.1
$\sigma_{c\delta t}$ [m]	1000	<i>Measurement standard deviation</i>	
σ_N [cycles]	1	σ_{pr} [m]	0.250
<i>Auto-correlation time scale</i>		σ_{cp} [m]	0.005
τ_a [s]	900		
$\tau_{c\delta t}$ [s]	60		

The following results are from satellite 1's filter, where the states of satellites 1 and 2 are estimated. Absolute and relative position errors for the 8-hour simulation are illustrated in Figure 12. Integer ambiguity resolution is employed after the filter approaches steady state, which occurs prior to the 1 hour mark. The relative position error shows the absolute position of satellite 1 subtracted from that of satellite 2, mapped into the RTN-frame of satellite 1. The achieved absolute navigation accuracy is below 1 m (1D, rms). This value is consistent with the accuracy of the broadcast ephemeris errors, which are the bottleneck on absolute accuracy. The relative navigation accuracy is below 1 cm (1D, rms) after IAR is activated. This is shown in all following results by a vertical red line, and marked in Figure 12 by a sudden decrease in the relative position error uncertainty bounds.

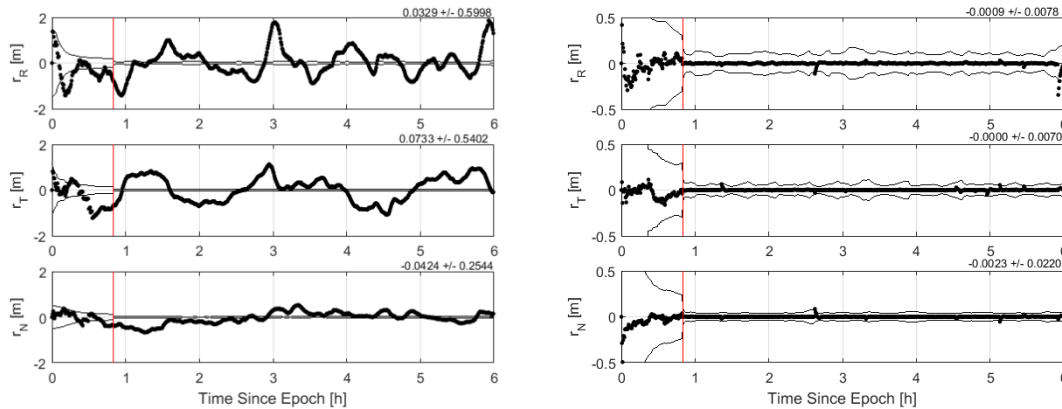


Figure 12: Absolute position error of satellite 1 (left) and relative position error of satellite 2 with respect to satellite 1 (right). Activation of IAR is shown by the red line.

The absolute and differential empirical acceleration estimates displayed alongside the true un-modeled accelerations is plotted in Figure 13. The un-modeled accelerations are taken from the truth simulation for comparison. The estimates broadly track the long periodic trends of the un-modeled accelerations, a positive confirmation of the filter performance.

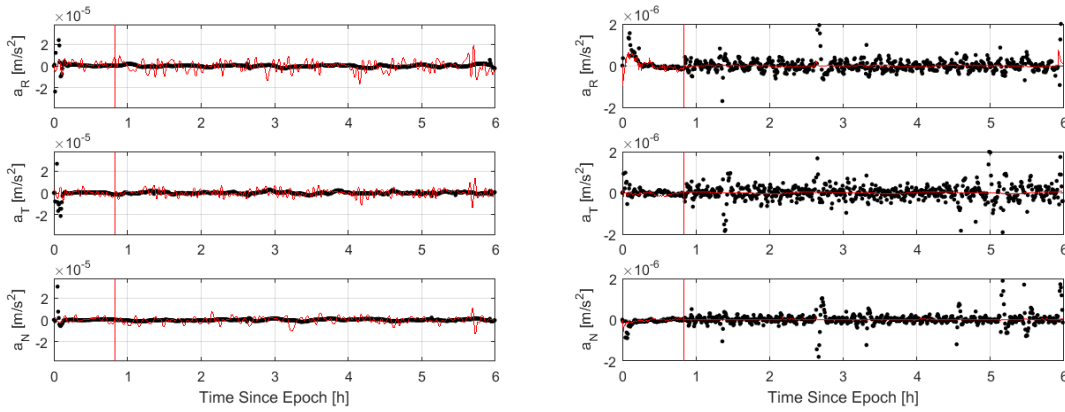


Figure 13: Absolute (left) and differential (right) empirical accelerations. Filter estimates (black) are compared to accelerations that are not modeled in the navigation filter (red).

The GRAPHIC and SDCP residuals are shown in Figure 14. They display banded Gaussian noise with standard deviations of 0.2 m and 3 cm, respectively. Prior to IAR, the standard deviation of the GRAPHIC measurements was 13 cm, and the standard deviation of the SDCP measurements was 1.1 mm. These noise values are consistent with the levels found during the Septentrio receiver characterization process (see Fig. 10).

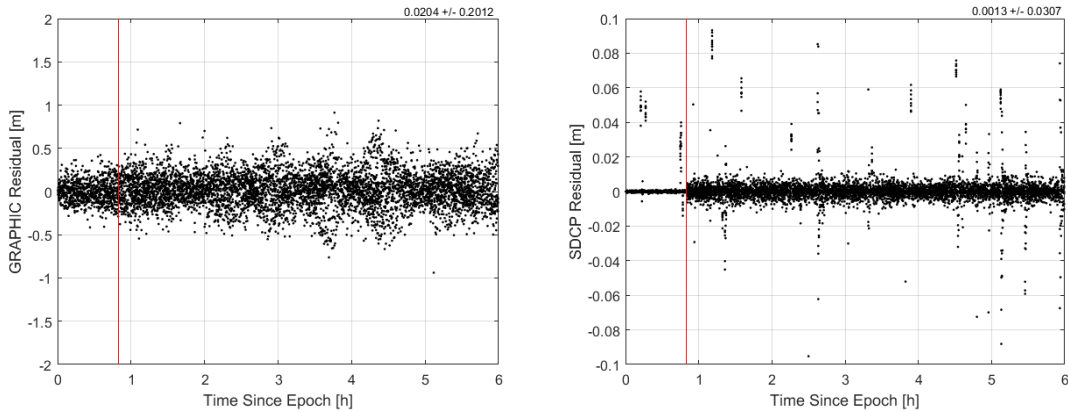


Figure 14: GRAPHIC (left) and SDCP (right) measurement residuals

Once satellite 1 estimates the state of its swarm subset, the relative estimates from the other subsets can be used to form full swarm knowledge. For example, the relative position between satellite 1 and 3 can be known by adding the relative state of 2 with respect to 1 (from satellite 1’s filter) to the relative state of 3 with respect to 2 (from satellite 2’s filter). The relative position between satellite 4 and 1 can be known by satellite 1 simply by taking the negative of the relative position of 1 with respect to 4, calculated in satellite 4’s filter. The resulting relative position errors of satellites 3 and 4 with respect to satellite 1 are shown in Figure 15. The steady-state estimate components show a maximum standard deviation of 6 cm, showing that the swarm determination slightly increases the error of relative estimates. This increase in error is because the correlation between the states is not considered, resulting in a factor of $\sqrt{2}$ increase as when adding random variables. However, covariance information from the filter can be used to exploit this correlation through covariance intersection and thus retain the high accuracy of individual DiGiTaL instances. It was also assumed that each spacecraft had ideal attitudes, and therefore many commonly visible GNSS satellites by the swarm. This allowed for the creation of several low-noise SDCP measurements in each filter. If the spacecraft had non-ideal attitudes, commonly visible satellites would be less abundant, resulting in fewer SDCP measurements and a less precise navigation solution. Therefore, for precision swarm navigation, the swarm subsets are chosen to maximize commonly visible GNSS satellites in each filter.

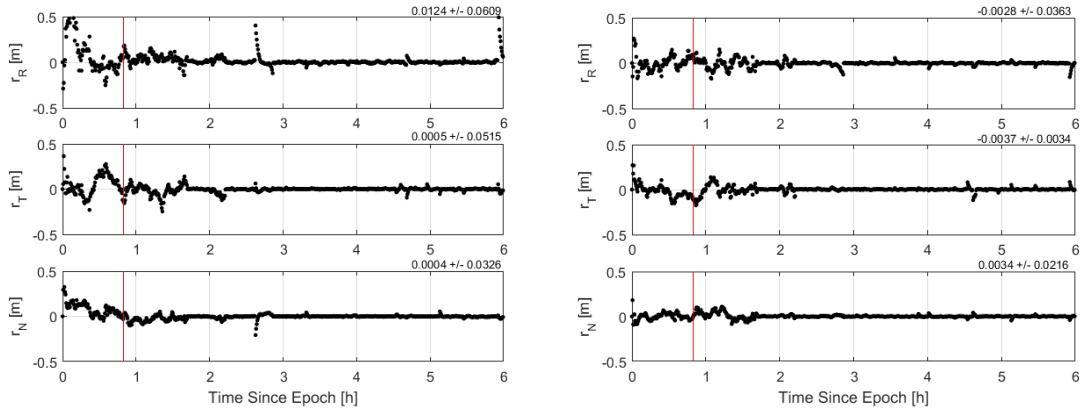


Figure 15: Relative position error of satellites 3 (left) and 4 (right) with respect to satellite 1 through swarm determination

Overall, these results are promising indicators that precision navigation of small satellite formations using the DiGiTaL is achievable, even in the case of a large swarm.

CONCLUSIONS AND FUTURE WORK

This paper presents the design and development of the Stanford GNSS and Radiofrequency Autonomous Navigation Testbed for DSS, which enables hardware-in-the-loop simulation of GNC systems for distributed space missions. The design of the testbed was divided into multiple sections. The first is the dynamic simulation, where satellite orbits are propagated through numerical integration of the equations of motions including all relative perturbation models. The second is signal generation, where RF signals are created either by a live roof antenna, or an IFEN GNSS signal simulator. The simulator is capable of reproducing signals for any desired scenario, enabling the testing of orbital navigation with input trajectory from the dynamics simulation. The third section of the testbed is measurement generation. This can be done in hardware, with incoming RF signals to a GNSS receiver, or entirely in software, where receiver trajectory information is provided to a software receiver emulator. The final block of the testbed is the navigation software, where algorithms and flight software can be validated either on a workstation or a flight computer for processor-in-the-loop testing.

To simulate the environmental conditions present in orbital scenarios, the Space Rendezvous Lab Satellite Software S^3 was developed. This high-performance software package uses the most recent models for orbit perturbations to enable high-fidelity simulation of large satellite formations. The dynamics propagation was compared with precise orbit products from the PRISMA mission, and found that the high-fidelity propagator was consistent to the accuracy of the flight products.

The receiver emulator and IFEN GSS were verified through a static test. The Septentrio roof antenna was used to collect a truth data set. The receiver emulator and GSS were then configured to reproduce the scenario through simulation. A cross-comparison was completed, and consistency was shown in tracking capabilities, signal carrier-to-noise ratios, and achievable navigation solutions. This comparison enabled the use of the GSS for receiver characterization through a zero-baseline test. The measurement noise characteristics of the Septentrio receiver were quantified, and the capability of the testbed to perform this characterization was shown.

Once developed and verified, the testbed was able to support the design and testing of the Distributed multi-GNSS Timing and Localization system. This project utilizes commercial-off-the-shelf hardware to create an onboard GNSS navigation payload for small satellite swarms, where each spacecraft is equipped with one DiGiTaL unit. When implemented, the navigation software divides the swarm into a smaller subset, and uses an Extended Kalman Filter to estimate the state of that subset. Information from each subset is then transmitted throughout the swarm, and full swarm knowledge is constructed. The formulation of this filter was presented, and a four-satellite HIL test scenario was conducted. Using both GRAPHIC and SDCP measurements with integer ambiguity resolution, navigation accuracies of <1 m and <1 cm were achieved for absolute and relative position, respectively.

The discussed DiGiTaL flight software is still in active development, so a closed-loop HIL test was not possible. In the near future, the flight software development will be completed and embedded into the Tyvak flatsat microprocessor. This will enable closed-loop HIL tests of precision navigation and control systems for small satellites. A CSAC will also be integrated into the DiGiTaL system to condition the GNSS receiver clock and enable precise time synchronization between multiple DiGiTaL units in a swarm.

Further algorithmic development of DiGiTaL includes improvements to integer ambiguity resolution techniques by using measurements from multiple GNSS constellations and across multiple frequencies to aid robustness and computational efficiency. Swarm topology will also be investigated, and methods for choosing the swarm subsets will be analyzed, such as maximization of the number of commonly visible GNSS satellites. Covariance intersection for swarm navigation will be addressed to better combine filter estimates by using all available information, compared with the current vector algebra approach. Other developmental areas include evaluation of different sources of error, such as broadcast ephemeris, multi-path, and Ionospheric delays, and using range-only measurements between spacecraft of the swarm for IAR initialization and in GNSS-impaired scenarios.

ACKNOWLEDGMENTS

The authors would like to thank The King Abdulaziz City for Science and Technology (KACST) Center of Excellence for research in Aeronautics & Astronautics (CEAA) at Stanford University for sponsoring this work. They would also like to thank the NASA Small Spacecraft Technology Program for funding the DiGiTaL project through grant number NNX16AT31A. The authors would like to acknowledge Duncan Eddy for his contributions to the testbed.

REFERENCES

- [1] B. Sullivan, D. Barnhart, L. Hill, P. Oppenheimer, B. L. Benedict, G. Van Ommering, L. Chappell, J. Ratti, and P. Will, "DARPA phoenix payload orbital delivery system (PODs): FedEx to GEO" *AIAA SPACE 2013 Conference and Exposition*, San Diego, California, 2013, p. 5484.
- [2] J. Kolmas, P. Banazadeh, A. W. Koenig, B. Macintosh, and S. D'Amico, "System design of a miniaturized distributed occulter/telescope for direct imaging of star vicinity," *2016 IEEE Aerospace Conference*, Big Sky, Montana, 2016, pp. 1-11.
- [3] O. Montenbruck, G. Allende-Alba, J. Rosello, M. Tossaint, and F. Zangerl, "Precise Orbit and Baseline Determination for the SAOCOM-CS Bistatic Radar Mission," *Proceedings of the 2017 International Technical Meeting of The Institute of Navigation*, Monterey, California, pp. 123-131.
- [4] S. D'Amico, J.-S. Ardaens, and R. Larsson, "Spaceborne autonomous formation-flying experiment on the PRISMA mission," *Journal of Guidance, Control, and Dynamics*, Vol. 35, No. 3, 2012, pp. 834-850.
- [5] O. Montenbruck, R. Kahle, S. D'Amico, and J.-S. Ardaens, "Navigation and control of the TanDEM-X formation," *The Journal of the Astronautical Sciences*, Vol. 56, No. 3, 2008, pp. 341-357.
- [6] S. Bandyopadhyay, G. P. Subramanian, R. Foust, D. Morgan, S.-J. Chung, and F. Hadaegh, "A review of impending small satellite formation-flying missions," *53rd AIAA Aerospace Sciences Meeting*, Kissimmee, Florida, 2015, p. 1623.
- [7] Roscoe, C., Westphal, J.J., and Bowen, J.A. "Overview and GNS design of the cubesat proximity operations demonstration (cpod) mission", *9th International Workshop on Satellite Constellations and Formation Flying*, University of Colorado Boulder, CO, 2017.
- [8] O. Montenbruck and R. Kroes, "In-flight performance analysis of the CHAMP BlackJack GPS Receiver," *GPS solutions*, Vol. 7, No. 2, 2003, pp. 74-86.
- [9] O. Montenbruck, M. Garcia-Fernandez, and J. Williams, "Performance comparison of semicodeless GPS receivers for LEO satellites," *GPS Solutions*, Vol. 10, No. 4, 2006, pp. 249-261.
- [10] V. Capuano, C. Botteron, and P.-A. Farine, "GNSS Performances for MEO, GEO and HEO," *64th International Astronautical Congress*, Beijing, China, 2013.
- [11] J. Leitner, "A hardware-in-the-loop testbed for spacecraft formation flying applications," *IEEE Aerospace Conference*, Vol. 2, 2001, pp. 615-620.
- [12] R. Burns, B. Naasz, D. Gaylor, and J. Higinbotham, "An environment for hardware-in-the-loop formation navigation and control," *AIAA/AAS Astrodynamics Specialist Conference and Exhibit*, Providence, Rhode Island, 2004, p. 4735.
- [13] E. Gill, B. Naasz, and T. Ebinuma, "First results from a hardware-in-the-loop demonstration of closed-loop autonomous formation flying," *26th Annual AAS Guidance and Control Conference*, Breckenridge, Colorado, 2003.
- [14] L. B. Winternitz, W. A. Bamford, S. R. Price, J. R. Carpenter, A. C. Long, and M. Farahmand, "Global Positioning System Navigation Above 76,000 km for NASA's Magnetospheric Multiscale Mission," *39th AAS Guidance, Navigation and Control Conference*, Breckenridge, Colorado, 2016.
- [15] S. Leung and O. Montenbruck, "Real-time navigation of formation-flying spacecraft using global-positioning-system measurements," *Journal of Guidance, Control, and Dynamics*, Vol. 28, No. 2, 2005, pp. 226-235.
- [16] S. D'Amico, S. De Florio, J.-S. Ardaens, and T. Yamamoto, "Offline and hardware-in-the-loop validation of the GPS-based real-time navigation system for the PRISMA formation flying mission," *3rd International Symposium on Formation Flying, Missions and Technology*, Noordwijk, Netherlands, 2008, pp. 23-25.

- [17] T. Yamamoto and S. D'Amico, "Hardware-in-the-loop demonstration of GPS-based autonomous formation flying," *4th ESA Workshop on Satellite Navigation User Equipment Technologies*, Noordwijk, Netherlands, 2008.
- [18] S. A. Kowalchuk, *Investigation of nonlinear control strategies using GPS simulator and spacecraft attitude control simulator*. PhD thesis, Virginia Polytechnic Institute and State University, 2007.
- [19] J.-I. Park, H.-E. Park, S.-Y. Park, and K.-H. Choi, "Hardware-in-the-loop simulations of GPS-based navigation and control for satellite formation flying," *Advances in Space Research*, Vol. 46, No. 11, 2010, pp. 1451-1465.
- [20] O. Montenbruck, M. Wermuth, A. Hauschild, G. Beyerle, A. Helm, S. Yudanov, A. Garcia, and L. Cacciapuoti, "Multi-GNSS Precise Orbit Determination of the International Space Station (ISS)," *2013 International Technical Meeting of The Institute of Navigation*, 2013, pp. 808-820.
- [21] S. Biswas, L. Qiao, and A. Dempster, "Space-borne GNSS based orbit determination using a SPIRENT GNSS simulator," *15th Australian Space Research Conference*, Adelaide, Australia, 2014.
- [22] S. D'Amico, R. C. Hunter, and C. Baker, "Distributed Timing and Localization (DiGiTaL)," ARC-E-DAA-TN45564, 2017.
- [23] B. D. Tapley, S. Bettadpur, M. Watkins, and C. Reigber, "The gravity recovery and climate experiment: Mission overview and early results," *Geophysical Research Letters*, Vol. 31, No. 9, 2004.
- [24] O. Montenbruck and E. Gill, *Satellite orbits*, Springer, Vol. 2, 2000, pp. 257-291.
- [25] J. Picone, A. Hedin, D. P. Drob, and A. Aikin, "NRLMSISE-00 empirical model of the atmosphere: Statistical comparisons and scientific issues," *Journal of Geophysical Research: Space Physics*, Vol. 107, No. A12, 2002.
- [26] W. M. Folkner, J. G. Williams, D. H. Boggs, R. S. Park, and P. Kuchynka, "The planetary and lunar ephemerides DE430 and DE431," *Interplanet. Netw. Prog. Rep.*, Vol. 196, 2014.
- [27] R. Kroes, *Precise relative positioning of formation flying spacecraft using GPS*. PhD thesis, TU Delft, Delft University of Technology, 2006.
- [28] G. Petit and B. Luzum, "IERS conventions (2010)," tech. rep., DTIC Document, 2010.
- [29] IAU SOFA Board, "IAU SOFA Software Collection,"
- [30] C. Bizouard and D. Gambis, "The combined solution C04 for Earth orientation parameters consistent with international terrestrial reference frame 2005," *Geodetic reference frames*, pp. 265-270, Springer, 2009.
- [31] Septentrio, "PolaNt Choke Ring B3/E6 High Precision Geodetic Choke Ring Antenna," datasheet, October 2015.
- [32] "IFEN Product Overview," <http://www.ifen.com/products/products-overview.html>. Accessed: 2016-11-30.
- [33] Novatel, "OEM 628 High Performance GNSS Receiver," D15588 datasheet, October 2016.
- [34] Septentrio, "AsteRx4 OEM Multi-frequency Dual-Antenna Receiver," datasheet, April 2016.
- [35] J. M. Dow, R. E. Neilan, and C. Rizos, "The international GNSS service in a changing landscape of global navigation satellite systems," *Journal of Geodesy*, Vol. 83, No. 3, 2009, pp. 191-198.
- [36] Jackson Labs, "Low Power Miniature RSR CSAC Time and Frequency Standard," 1005120 datasheet, July 2017.
- [37] "Spectracom TSync Product Page," <https://spectracom.com/products-services/precision-timing/tsync-timecode-reprocessors>. Accessed: 2017-04-26.
- [38] J.-S. Ardaens, O. Montenbruck, and S. D'Amico, "Functional and performance validation of the PRISMA precise orbit determination facility," *ION International Technical Meeting*, San Diego, California, 2010, pp. 25-27.
- [39] J.-S. Ardaens, S. D'Amico, and O. Montenbruck, "Final commissioning of the PRISMA GPS navigation system," *Journal of Aerospace Engineering*, Vol. 4, No. 3, 2012, p. 105.
- [40] N. R. Canada, "Online Global GPS Processing Service (CSRS-PPP)," 2010. Natural Resources Canada. Online Global GPS Processing Service (CSRS-PPP). <http://www.geod.nrcan.gc.ca/products/products/pppe.php> (2010).
- [41] P. Tetrault and P. Sauve, "CSRS-PPP: A web tool to facilitate NAD83(CSRS) integration," tech. rep., Ontario Professional Surveyor, 2010.
- [42] T. Yunck, *Coping with the Atmosphere and Ionosphere in Precise Satellite and Ground Positioning in: Environmental Effects on Spacecraft Trajectories and Positioning*. Washington, D.C., American Geophysical Union, 1993.
- [43] MOPS, *Minimum Operational Performance Standards for Global Positioning System/Wide Area Augmentation System Airborne Equipment*. Document No. RTCA/DO-229A, 1998.
- [44] A. E. Niell, "Global mapping functions for the atmosphere delay at radio wavelengths," *Journal of Geophysical Research*, Vol. 101, 1996, pp. 3227-3246.
- [45] S. D'Amico, *Autonomous Formation Flying in Low Earth Orbit*. PhD thesis, TU Delft, Delft University of Technology, 2010.
- [46] O. Montenbruck and C. Renaudie, "Phoenix-S/-XNS performance validation," DLR/GSOC GTN-TST-0120, 2007.
- [47] P. Ward, *Satellite Signal Acquisition and Tracking, in Understanding GPS, Principle and Applications*. Kaplan, 2006.
- [48] X. W. Chang, X. Wang, and T. Zhou, "MLAMBDA: a modified LAMBDA method for integer least-squares estimation," *Journal of Geodesy*, Vol. 79, No. 9, 2005, pp. 552-565.